Additive Manufacturing 84 (2024) 104079

Contents lists available at ScienceDirect

Additive Manufacturing

journal homepage: www.elsevier.com/locate/addma

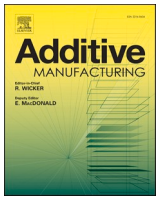

Solute segregation in a rapidly solidified Hastelloy-X Ni-based superalloy during laser powder bed fusion investigated by phase-field and computational thermal-fluid dynamics simulations

Masayuki Okugawa [a,b,*], Kenji Saito [a], Haruki Yoshima [a], Katsuhiko Sawaizumi [a], Sukeharu Nomoto [c], Makoto Watanabe [c], Takayoshi Nakano [a,b], Yuichiro Koizumi [a,b,*]

[a] Graduate School of Engineering, Osaka University, 2-1 Yamadaoka, Suita, Osaka 565-0871, Japan
[b] Anisotropic Design & Additive Manufacturing Research Center, Osaka University, Suita 565-0871, Japan
[c] Research Center for Structural Materials, National Institute for Materials Science, Ibaraki 305-0047, Japan

ARTICLE INFO

Keywords:
Laser powder-bed fusion
Hastelloy-X nickel-based superalloy
Solute element segregation
Computational thermal-fluid dynamics simulation
Phase-field method

ABSTRACT

Solute segregation significantly affects material properties and is a critical issue in the laser powder-bed fusion (LPBF) additive manufacturing (AM) of Ni-based superalloys. To the best of our knowledge, this is the first study to demonstrate a computational thermal-fluid dynamics (CtFD) simulation coupled multi-phase-field (MPF) simulation with a multicomponent-composition model of Ni-based superalloy to predict solute segregation under solidification conditions in LPBF. The MPF simulation of the Hastelloy-X superalloy reproduced the experimentally observed submicron-sized cell structure. Significant solute segregations were formed within interdendritic regions during solidification at high cooling rates of up to 1.6×10^6 K s^{-1}, a characteristic feature of LPBF. Solute segregation caused a decrease in the solidus temperature (T_S), with a reduction of up to 38.4 K, which increases the risk of liquation cracks during LPBF. In addition, the segregation triggers the formation of carbide phases, which increases the susceptibility to ductility dip cracking. Conversely, we found that the decrease in T_S is suppressed at the melt-pool boundary regions, where re-remelting occurs during the stacking of the layer above. Controlling the re-remelting behavior is deemed to be crucial for designing crack-free alloys. Thus, we demonstrated that solute segregation at the various interfacial regions of Ni-based multicomponent alloys can be predicted by the conventional MPF simulation. The design of crack-free Ni-based superalloys can be expedited by MPF simulations of a broad range of element combinations and their concentrations in multicomponent Ni-based superalloys.

1. Introduction

Additive manufacturing (AM) technologies have attracted considerable attention as they allow us to easily build three-dimensional (3D) parts with complex geometries. Among the wide range of available AM techniques, laser powder-bed fusion (LPBF) has emerged as a preferred technique for metal AM [1–5]. In LPBF, metal products are built layer-by-layer by scanning laser, which fuse metal powder particles into bulk solids.

Significant attempts have been made to integrate LPBF techniques within the aerospace industry, with a particular focus on weldable Ni-based superalloys, such as IN718 [6–8], IN625 [9,10], and Hastelloy-X (HX) [11–14]. Non-weldable alloys, such as IN738LC [15,16] and CMSX-4 [1,17] are also suitable for their sufficient creep resistance under higher temperature conditions. However, non-weldable alloys are difficult to build using LPBF because of their susceptibility to cracking during the process. In general, a macro solute-segregation during solidification is suppressed by the rapid cooling conditions (up to 10^8 K s^{-1}) unique to the LPBF process [18]. However, the solute segregation still occurs in the interdendritic regions that are smaller than the micrometer scale [5,19–21]; these regions are suggested to be related to the hot cracks in LPBF-fabricated parts. Therefore, an understanding of solute segregation is essential for the fabrication of reliable LPBF-fabricated parts while avoiding cracks.

The multiphase-field (MPF) method has gained popularity for modeling the microstructure evolution and solute segregation under

* Corresponding authors at: Graduate School of Engineering, Osaka University, 2-1 Yamadaoka, Suita, Osaka 565-0871, Japan.
E-mail addresses: okugawa@mat.eng.osaka-u.ac.jp (M. Okugawa), ykoizumi@mat.eng.osaka-u.ac.jp (Y. Koizumi).

https://doi.org/10.1016/j.addma.2024.104079
Received 19 September 2023; Received in revised form 4 February 2024; Accepted 9 March 2024
Available online 11 March 2024

Table 1
Parameters used in the CtFD simulations.

Parameter	Symbol	Value	Reference
Density at 298.15 K	ρ	8.24 g cm^{-3}	[*]
Liquidus temperature	T_L	1628.15 K	[*]
Solidus temperature	T_S	1533.15 K	[*]
Viscosity at T_L	η	6.8 g m^{-1} s^{-1}	[*]
Specific heat at 298.15 K	C_P	0.439 J g^{-1} K^{-1}	[*]
Thermal conductivity at 298.15 K	λ	10.3 W m^{-1} K^{-1}	[*]
Surface tension at T_L	γ_L	1.85 J m^{-2}	[*]
Temperature coefficient of surface tension	$d\gamma_L/dT$	-2.5×10^{-4} J m^{-2} K^{-1}	[*]
Emissivity	E	0.27	[31]
Stefan–Boltzmann constant	σ	5.67×10^{-8} W m^{-2} K^{-4}	[31]
Heat of fusion	ΔH_{SL}	2.76×10^{2} J g^{-1}	[32]
Heat of vaporization	ΔH_{LV}	4.29×10^{3} J g^{-1}	[32]
Vaporization temperature	T_V	3110 K	[32]

[*] Calculated using JMatPro v11.

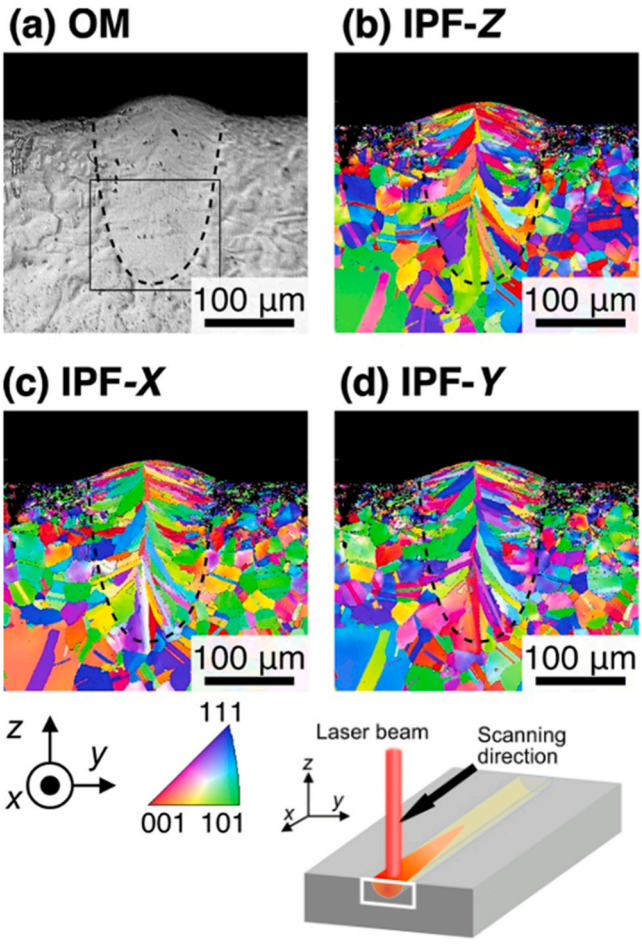

Fig. 1. (a) Optical microscopy image and SEM-EBSD (b) IPF-Z, (c) IPF-X, and (d) IPF-Y maps of the cross-section of melt region.

rapid cooling conditions [5,20–28]. Moreover, quantifiable predictions have been achieved by combining the MPF method with temperature distribution analysis methods such as the finite-element method (FEM) [20] and computational thermal-fluid dynamics (CtFD) simulations [28]. These aforementioned studies have used binary-approximated multicomponent systems, such as Ni–Nb binary alloys, to simulate IN718 alloys. While MPF simulations using binary alloy systems can effectively reproduce microstructure formations and segregation behaviors, the binary approximation might be affected by the chemical interactions between the removed solute elements in the target multicomponent alloy. The limit of absolute stability predicted by the Mullins-Sekerka theory [29] is also crucial because the limit velocity is close to the solidification rate in the LPBF process and is different in multicomponent and binary-approximated systems. The difference between the solidus and liquidus temperatures, ΔT_0, directly determines the absolute stability according to the Mullins-Sekerka theory. For example, the ΔT_0 values of IN718 and its binary-approximated Ni–5 wt %Nb alloy are 134 K [28] and 71 K [30], respectively. The solidification rate compared to the limit of absolute stability, i.e., the relative non-equilibrium of solidification, changes by simplification of the system. It is therefore important to use the composition of the actual multicomponent system in such simulations. However, to the best of our knowledge, there is no MPF simulation using a multicomponent model coupled with a temperature analysis simulation to predict solute segregation in a Ni-based superalloy.

In this study, we demonstrate that the conventional MPF model can reproduce experimentally observed dendritic structures by performing a phase-field simulation using the temperature distribution obtained by a CtFD simulation of a multicomponent Ni-based alloy (conventional solid-solution hardening-type HX). The MPF simulation revealed that the segregation behavior of solute elements largely depends on the regions of the melt pool, such as the cell boundary, the interior of the melt-pool boundary, and heat-affected regions. The sensitivities of the various interfaces to liquation and solidification cracks are compared based on the predicted concentration distributions. Moreover, the feasibility of using the conventional MPF model for LPBF is discussed in terms of the absolute stability limit.

2. Methods

2.1. Laser-beam irradiation experiments

Rolled and recrystallized HX ingots with dimensions of 20 × 50 × 10 mm were used as the specimens for laser-irradiation experiments. The specimens were irradiated with a laser beam scanned along straight lines of 10 mm in length using a laser AM machine (EOS 290 M, EOS) equipped with a 400 W Yb-fiber laser. Irradiation was performed with a beam power of $P = 300$ W and a scanning speed of $V = 600$ mm s^{-1}, which are the conditions generally used in the LPBF fabrication of Ni-based superalloy [8]. The corresponding line energy was 0.5 J mm^{-1}. The samples were cut perpendicular to the beam-scanning direction for cross-sectional observation using a field-emission scanning electron microscope (FE-SEM, JEOL JSM 6500). Crystal orientation analysis was performed by electron backscatter diffraction (EBSD). The sizes of each crystal grain and their aspect ratios were evaluated by analyzing the EBSD data.

2.2. CtFD simulation

CtFD simulations of the laser-beam irradiation of HX were performed using a 3D thermo-fluid analysis software (Flow Science FLOW-3D® with Flow-3D Weld module). A Gaussian heat source model was used, in which the irradiation intensity distribution of the beam is regarded as a symmetrical Gaussian distribution over the entire beam. The distribution of the beam irradiation intensity is expressed by the following equation.

$$\dot{q} = \frac{2\eta P}{\pi R^2} \exp\left(-\frac{2r^2}{R^2}\right). \quad (1)$$

Here, P is the power, R is the effective beam radius, r is the actual beam radius, and η is the beam absorption rate of the substrate. To improve the accuracy of the model, η was calculated by assuming multiple reflections using the Fresnel equation:

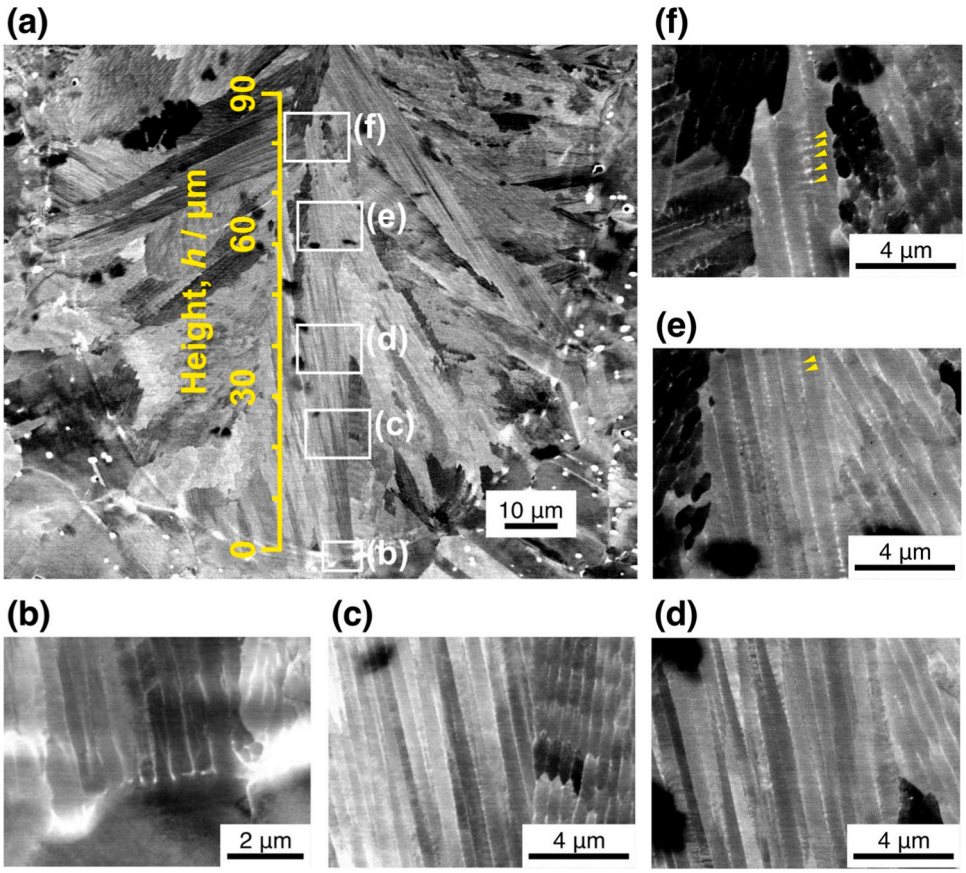

Fig. 2. Backscattered electron images of (a) lower half of the melt pool (black square area in Fig. 1a), (b) bottom of the melt pool, and at heights of (c) 20, (d) 40, (e) 60, and (f) 80 μm from the bottom of the melt pool.

$$\eta = 1 - \frac{1}{2}\left\{\frac{1+(1-\varepsilon\cos\theta)^2}{1+(1+\varepsilon\cos\theta)^2} + \frac{\varepsilon^2 - 2\varepsilon\cos\theta + 2\cos^2\theta}{\varepsilon^2 + 2\varepsilon\cos\theta + 2\cos^2\theta}\right\}. \quad (2)$$

ε is the Fresnel coefficient and θ is the incident angle of the laser. A local laser melt causes the vaporization of the material and results in a high vapor pressure. This vapor pressure acts as a recoil pressure on the surface, pushing the weld pool down. The recoil pressure is reproduced using the following equation.

$$p_{\text{recoil}} = Ap_0\exp\left[\frac{\Delta H_{\text{LV}}}{RT_{\text{V}}}\left(1 - \frac{T_{\text{V}}}{T}\right)\right]. \quad (3)$$

Here, p_0 is the atmospheric pressure, ΔH_{LV} is the latent heat of vaporization, R is the gas constant, and T_{V} is the boiling point at the saturated vapor pressure. A is a ratio coefficient that is generally assumed to be 0.54, indicating that the recoil pressure due to evaporation is 54% of the vapor pressure at equilibrium on the liquid surface.

Table 1 shows the parameters used in the simulations. Most parameters were evaluated using an alloy physical property calculation software (Sente software JMatPro v11). The values in a previously published study [31] were used for the emissivity and the Stefan–Boltzmann constant, and the values for pure Ni [32] were used for the heat of vaporization and vaporization temperatures. The Fresnel coefficient, which determines the beam absorption efficiency, was used as a fitting parameter to reproduce the morphology of the experimentally observed melt region, and a Fresnel coefficient of 0.12 was used in this study.

The dimensions of the computational domain of the numerical model were 4.0 mm in the beam-scanning direction, 0.4 mm in width, and 0.3 mm in height. A uniform mesh size of 10 μm was applied throughout the computational domain. The boundary condition of continuity was applied to all boundaries except for the top surface. The temperature was initially set to 300 K. P and V were set to their experimental values, i.e., 300 W and 600 mm s^{-1}, respectively. Solidification conditions based on the temperature gradient, G, the solidification rate, R, and the cooling rate were evaluated, and the obtained temperature distribution was used in the MPF simulations.

2.3. MPF simulation

Two-dimensional MPF simulations weakly coupled with the CtFD simulation were performed using the Microstructure Evolution Simulation Software (MICRESS) [33–37] with the TQ-Interface for Thermo-Calc [38]. A simplified HX alloy composition of Ni-21.4Cr-17.6Fe-0.46Mn-8.80Mo-0.39Si-0.50 W-1.10Co-0.08 C (mass %) was used in this study. The Gibbs free energy and diffusion coefficient of the system were calculated using the TCNI9 thermodynamic database [39] and the MOBNi5 mobility database [40]. The equilibrium phase diagram calculated using Thermo-Calc indicates that the face-centered cubic (FCC) and σ phases appear as the equilibrium solid phases [19]. However, according to the time-temperature-transformation (*TTT*) diagram [41], the phases are formed after the sample is maintained for tens of hours in a temperature range of 1073–1173 K. Therefore, only the liquid and FCC phases were assumed to appear in the MPF simulations. The simulation domain was 5 × 100 μm, and the grid size Δx and interface width were set to 0.025 and 0.1 μm, respectively. The interfacial mobility between the solid and liquid phases was set to 1.0×10^{-8} m^4 J^{-1} s^{-1}. Initially, one crystalline nucleus with a [100] crystal orientation was placed at the left bottom of the simulation domain, with the liquid phase occupying the remainder of the domain. The model was solidified under the temperature field distribution obtained by the CtFD simulation. The concentration

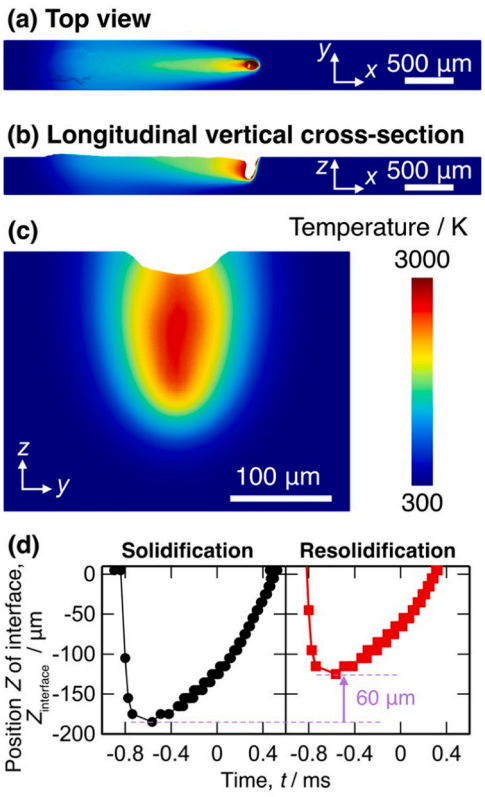

Fig. 3. (a–c) Snapshots of the CtFD simulation of laser-beam irradiation: (a) Top, (b) longitudinal vertical cross-sectional, and (c) transversal vertical cross-sectional views. (d) z-position of the solid/liquid interface during melting and solidification.

distribution and crystal orientation of the solidified model were examined. The primary dendrite arm space (PDAS) was compared to the experimental PDAS measured by the cross-sectional SEM observation.

In an actual LPBF process, solidified layers are remelted and resolidified during the stacking of the one layer above, thereby greatly affecting solute element distributions in those regions. Therefore, remelting and resolidification simulations were performed to examine the effect of remelting on solute segregation. The solidified model was remelted and resolidified by applying a time-dependent temperature field shifted by 60 μm in the height direction, assuming reheating during the stacking of the upper layer (i.e., the upper 40 μm region of the simulation box was remelted and resolidified). The changes in the composition distribution and formed microstructure were investigated.

3. Results

3.1. Experimental observation of melt pool

Fig. 1 shows a cross-sectional optical microscopy image and corresponding inverse pole figure (IPF) orientation maps obtained from the laser-melted region of HX. The dashed line indicates the fusion line. A deep melted region was formed by keyhole-mode melting due to the vaporization of the metal and resultant recoil pressure. Epitaxial growth from the unmelted region was observed. Columnar crystal grains with an average diameter of 5.46 ± 0.32 μm and an aspect ratio of 3.61 ± 0.13 appeared at the melt regions (Figs. 1b–1d). In addition, crystal grains growing in the *z* direction could be observed in the lower center.

Fig. 2a shows a cross-sectional backscattering electron image (BEI) obtained from the laser-melted region indicated by the black square in Fig. 1a. The bright particles with a diameter of approximately 2 μm observed outside the melt pool. It is well known that M_6C, $M_{23}C_6$, σ, and μ precipitate phases are formed in Hastelloy-X [41]. These precipitates

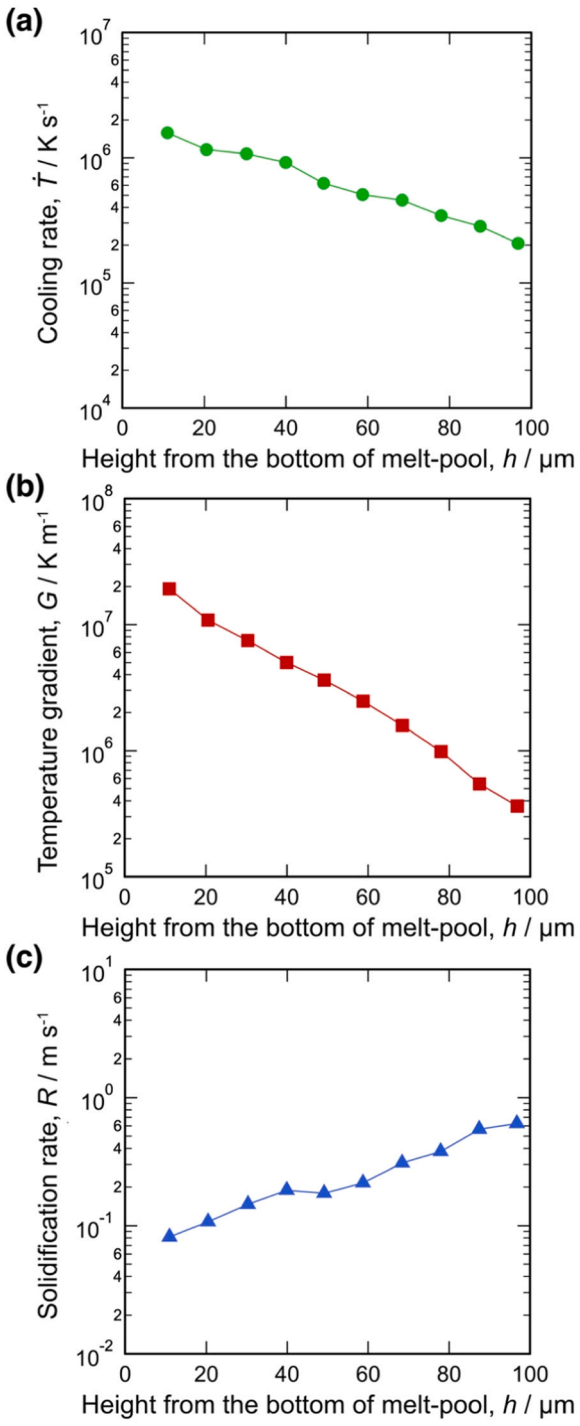

Fig. 4. (a) Cooling rate, (b) temperature gradient, and (c) solidification rate at the solid/liquid interface as a function of the height from the bottom of the melt pool, evaluated from the temperature distributions by the CtFD simulation.

mainly consisted of Mo, Cr, Fe, and Ni; The μ and M_6C phases are rich in Mo, while the σ and $M_{23}C_6$ phases are rich in Cr. The SEM energy dispersive X-ray spectroscopy analysis suggested that the bright particles are the stable precipitates as shown in Fig. S2 and Table S1. Conversely, there are no carbides in the melt pool. This suggests that the cooling rate is extremely high during LPBF, which prevents the formation of a stable carbide during solidification. Figs. 2b–2f show magnified BEI images at different height positions indicated in Fig. 2a. Bright regions are observed between the cells, which become fragmentary at the center of the melt pool, as indicated by the yellow arrow heads in

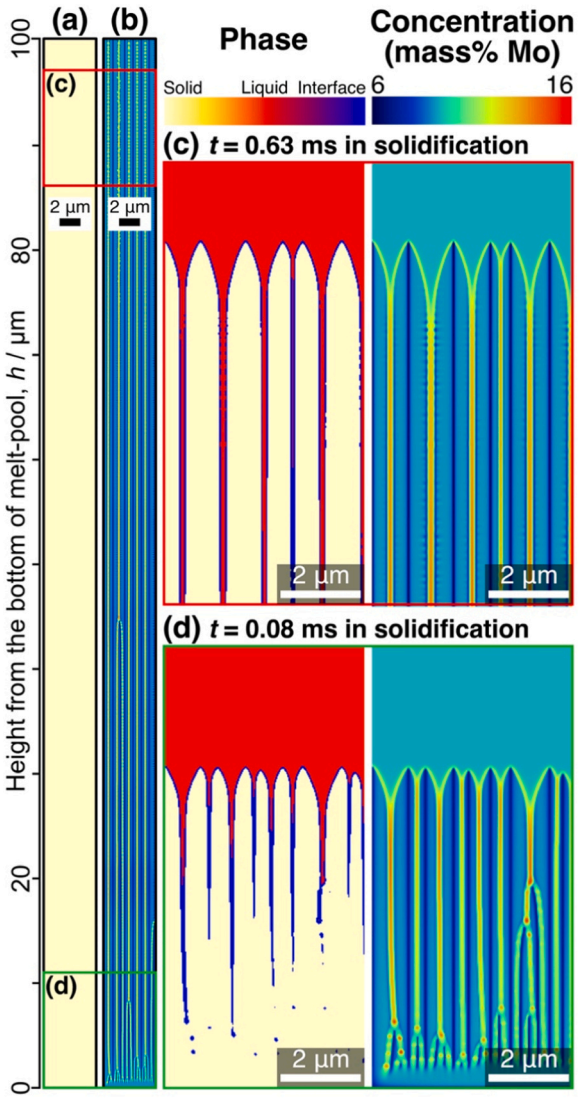

Fig. 5. MPF solidified models colored by (a) phase and (b) Mo concentration. (c, d) the magnified images during the solidification of the regions indicated by rectangles in (a) and (b).

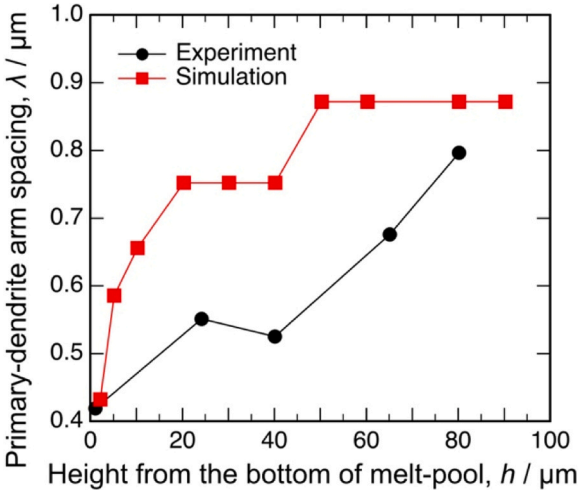

Fig. 6. PDAS as a function of the height from the bottom of the melt pools obtained by experiments and MPF simulations.

Figs. 2e and 2f.

3.2. CtFD simulation

Fig. 3a–c show snapshots of the CtFD simulation of HX at 2.72 ms, with the temperature indicated in color. A melt pool with an elongated teardrop shape formed and keyhole-mode melting was observed at the front of the melt region. The cooling rate, temperature gradient (G), and solidification rate (R) were evaluated from the temporal change in the temperature distribution of the CtFD simulation results. The z-position of the solid/liquid interface during the melting and solidification processes is shown in Fig. 3d. The interface goes down rapidly during melting and then rises during solidification. The MPF simulation of the microstructure formation during solidification was performed using the temperature distribution. Moreover, the microstructure formation process during the fabrication of the upper layer was investigated by remelting and resolidifying the solidified layer using the same temperature distribution with a 60 μm upward shift, corresponding to the layer thickness commonly used in the LPBF of Ni-based superalloys.

Fig. 4a–c show the changes in the cooling rate, temperature gradient, and solidification rate in the center line of the melt pool parallel to the z direction. To output the solidification conditions at the solid/liquid interface in the melt pool, only the data of the mesh where the solid phase ratio was close to 0.5 were plotted. Solidification occurred where the cooling rate was in the range of 2.1×10^5–1.6×10^6 K s^{-1}, G was in the range of 3.6×10^5–1.9×10^7 K m^{-1}, and R was in the range of 8.2×10^{-2}–6.3×10^{-1} m s^{-1}. The cooling rate was the highest near the fusion line and decreased as the interface approached the center of the melt region (Fig. 4a). G also exhibited the highest value in the regions near the fusion line and decreased throughout the solid/liquid interface toward the center of the melt pool (Fig. 4b). R had the lowest value near the fusion line and increased as the interface approached the center of the melt region (Fig. 4c).

3.3. MPF simulations coupled with CtFD simulation

MPF simulations of solidification, remelting, and resolidification were performed using the temperature-time distribution obtained by the CtFD simulation. Fig. 5 shows the MPF solidified models colored by phase and Mo concentration. All the computational domains show the FCC phase after the solidification (Fig. 5a). Dendrites grew parallel to the heat flow direction, and solute segregations were observed in the interdendritic regions. At the bottom of the melt pool (Fig. 5d), planar interface growth occurred before the formation of primary dendrites. The bottom of the melt pool is the turning point of the solid/liquid interface from the downward motion in melting to the upward motion in solidification. Thus, the solidification rate at the boundary is zero, and is extremely low immediately above the molt-pool boundary. Here, the lower limit of the solidification rate (R) for dendritic growth can be represented by the constitutional supercooling criterion [29], $V_{cs} = (G \times D_L) / \Delta T$, and planar interface growth occurs at $R < V_{cs}$. D_L and ΔT denote the diffusion coefficient in the liquid and the equilibrium freezing range, respectively. The results suggest that planar interface growth occurs at the bottom of the melt pool, resulting in a dark region with a different solute element distribution. Some of the primary dendrites were diminished by competition with other dendrites. In addition, secondary dendrite arms could be seen in the upper regions (Fig. 5c), where solidification occurred at a lower cooling rate. The fragmentation of the solute segregation near the secondary dendrite arms is similar to that observed in the experimental melt pool shown in Figs. 2e and 2f, and the secondary dendrite arms are suggested to have appeared at the center of the melt region. Fig. 6 shows the PDASs measured from the MPF simulation models, compared to the experimental PDASs measured by the cross-sectional SEM observation of the laser-melted regions (Fig. 2). The PDAS obtained by the MPF simulation becomes larger as the solidification progress. Ghosh et al. [21] revealed by the phase-field

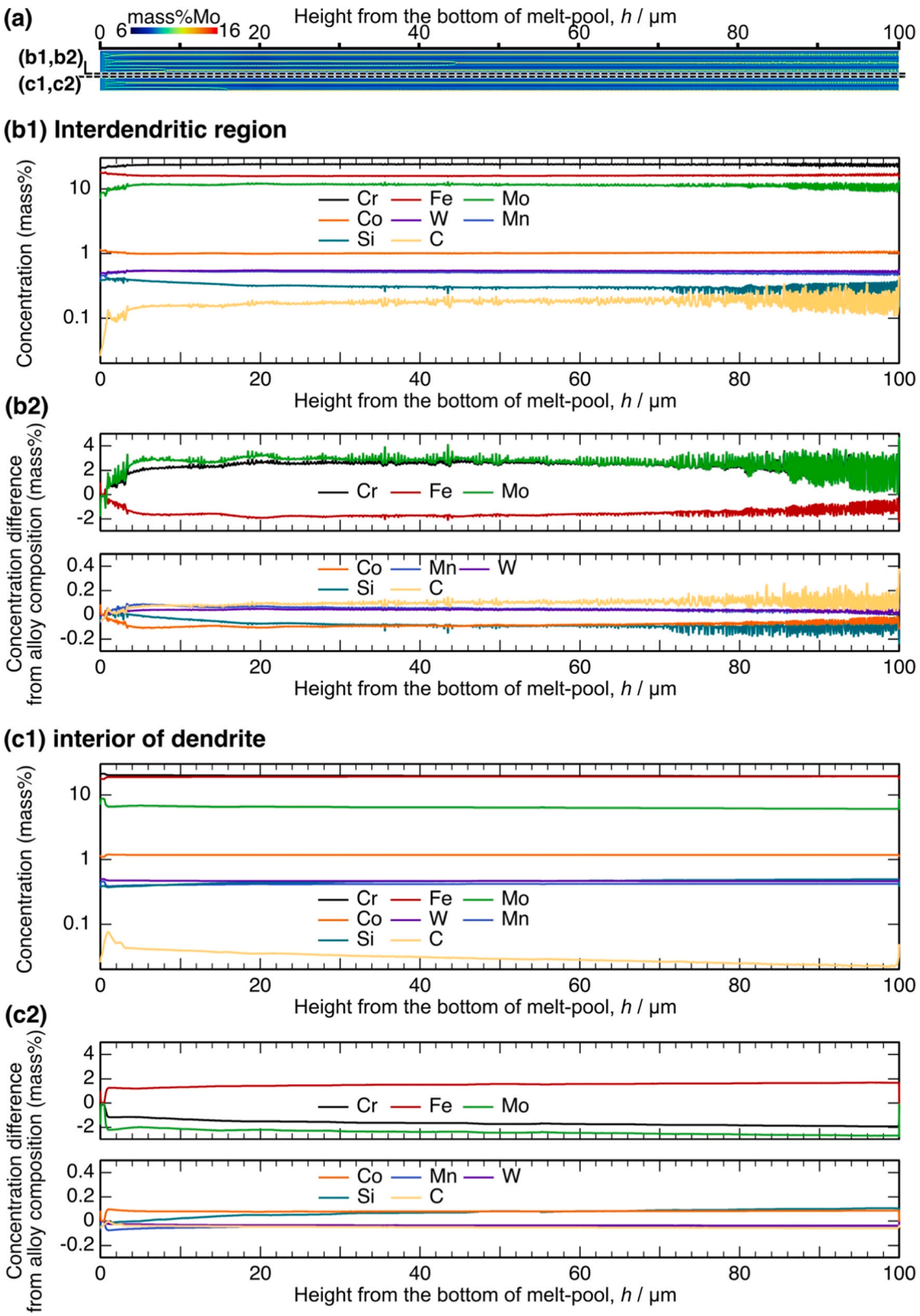

Fig. 7. (a) Solidified model with Mo concentration in color. (b1–c2) Concentration profiles of the MPF solidified model indicated by arrows in (a): (b1, b2) interdendritic region and (c1, c2) interior of the dendrite.

method that the PDAS decreases as the cooling rate increases under the rapid cooling conditions obtained by the finite element analysis. In this study, the cooling rate decreased as the interface approached the center of the melt region (Fig. 4a), and the trends in PDAS change with respect to cooling rate is same as the reported trend [21]. The simulated trends of the PDAS with the position in the melt pool agreed well with the experimental trends. However, all PDASs in the simulation were larger than those observed in the experiment at the same positions. Ode et al.

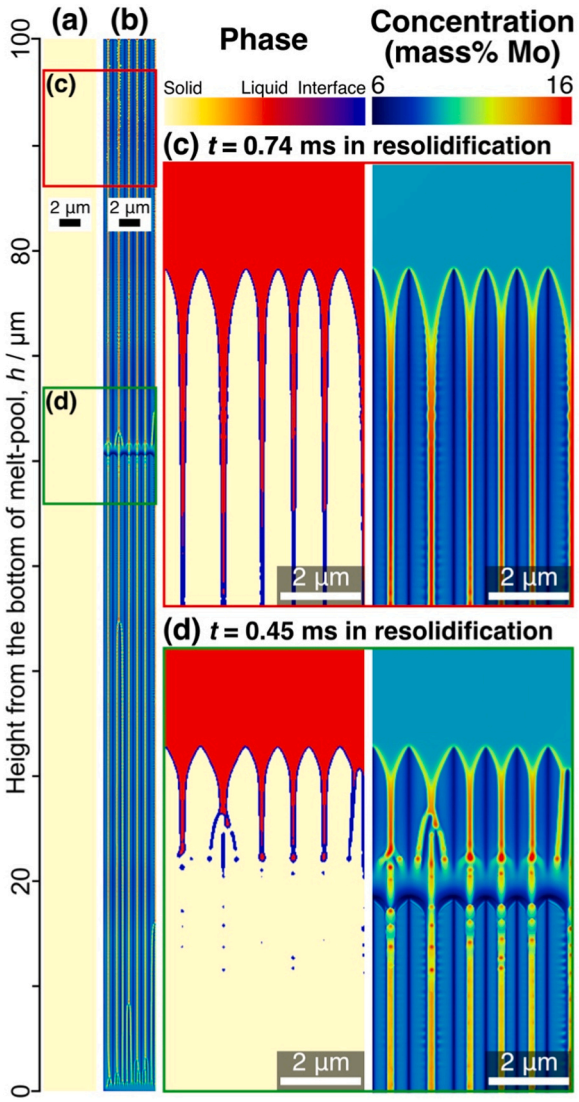

Fig. 8. MPF resolidified models colored by (a) phase and (b) Mo concentration. (c, d) MPF resolidified models during the resolidification of the regions indicated by rectangles in (a) and (b).

[42] reported that PDAS differences between 2D and 3D MPF simulations can be represented by $PDAS_{2D} = 1.12 \times PDAS_{3D}$ owing to differences in the effects of the interfacial energy and diffusivity. We also performed 2D and 3D MPF simulations under the solidification conditions of $G = 1.94 \times 10^7$ K m^{-1} and $R = 0.82$ m s^{-1} (Fig. S1), and found that the PDAS from the 2D MPF simulation was 1.26 times larger than that from the 3D simulation. Therefore, the cell structure obtained by the CtFD simulation coupled with the 2D MPF simulation agreed well with the experimental results over the entire melt pool region considering the dimensional effects.

Fig. 7b1 and c1 show the concentration profiles of the solidified model along the growth direction indicated by dashed lines in Fig. 7a. The differences in concentrations from the alloy composition are also shown in Fig. 7b2 and c2. Cr, Mo, C, Mn, and W were segregated to the interdendritic regions, while Si, Fe, and Co were depressed. The solute segregation behavior agrees with the experimental observation [43] and the prediction by the Scheil-Gulliver simulation [19]. Segregation occurred to the highest degree in Mo, while the ratio of segregation to the alloy composition was remarkable in C. The concentration fluctuations correlated with the position in the melt pool and decreased at the center of the melt pool, which was suggested to correspond to the lower cooling rate in this region. Conversely, droplets that appeared between secondary dendrite arms in the upper regions of the simulation domain exhibited a locally high segregation of solute elements, with the same amount of segregation as that at the bottom of the melt pool.

3.4. Remelting and resolidification simulation

The solidified model was subjected to remelting and resolidification conditions by shifting the temperature profile upward by 60 μm to reveal the effect of reheating on the solute segregation behavior. Fig. 8a and b shows the simulation domains of the HX model after resolidification, colored by phase and Mo concentration. The magnified MPF models during the resolidification of the regions indicated by rectangles in Fig. 8a and b are also shown as Fig. 8c and d. Dendrites grew from the bottom of the remelted region, with the segregation of solute elements occurring in the interdendritic regions. The entire domain become the FCC phase after the resolidification, as shown in Fig. 8a. The bottom of the remelted regions exhibited a different microstructure, and Mo was depressed at the remelted regions, rather than the interdendritic regions. The different solute segregation behavior [44] and the microstructure formation [45] at the melt pool boundary is also observed in LPBF manufactured 316 L stainless steel. We found that this microstructure was formed by further remelting during the resolidification process, which is shown in Fig. 9. Here, the solidified HX model was heated, and the interdendritic regions were preferentially melted while concentration fluctuations were maintained (Fig. 9a1 and a2). Subsequently, planer interface growth occurs near the melt pool boundary where the solidification rate is almost zero, and the dendrites outside of the boundary are grown epitaxially (Fig. 9b1 and b2). However, these remelted again because of the temperature rise (Fig. 9c1 and c2, and the temperature-time profile shown in Fig. 9e). The remelted regions then cooled and solidified with the abnormal solute segregations (Fig. 9d1 and d2). Then, dendrite grows from amplified fluctuations under the solidification rate larger than the criterion of constitutional supercooling (Fig. 9d1, 9d2, and Fig. 8d). It has been reported [46,47] that temperature rising owning to latent heat affects microstructure formation: phase-field simulations of a Ni–Al binary alloy suggest that the release of latent heat during solidification increases the average temperature of the system [46] and strongly influences the solidification conditions [47]. In this study, the release of latent heat during solidification is considered in CtFD simulations for calculating the temperature distribution, and the temperature increase is suggested to have also occurred due to the release of latent heat.

Fig. 10b1 and 1c1 show the solute element concentration line profiles of the resolidified model along the growth direction indicated by dashed lines in Fig. 10a. Fig. 10b2 and 10c2 show the corresponding differences in concentration from the alloy composition. The segregation behavior of solute elements at the interdendritic regions (Fig. 10b1 and 10b2) was the same as that in the solidified model (Figs. 7b1 and 7b2). Here, Cr, Mo, C, Mn, and W were segregated to the interdendritic regions, while Si, Fe, and Co were depressed. However, the concentration fluctuations at the interdendritic regions were larger than those in the solidified model. Moreover, the segregation of the outside of the melt pool, i.e., the heat-affected zone, was remarkable throughout remelting and resolidification. Different segregation behaviors were observed in the re-remelted region: Mo, Si, Mn, and W were segregated, while Ni, Fe, and Co were depressed. These solute segregations caused by remelting are expected to heavily influence the crack behavior.

4. Discussion

4.1. Effect of segregation of solute elements on liquation cracking susceptibility

Strong solute segregation was observed between the interdendritic regions of the solidified alloy (Fig. 7). In addition, the solute segregation

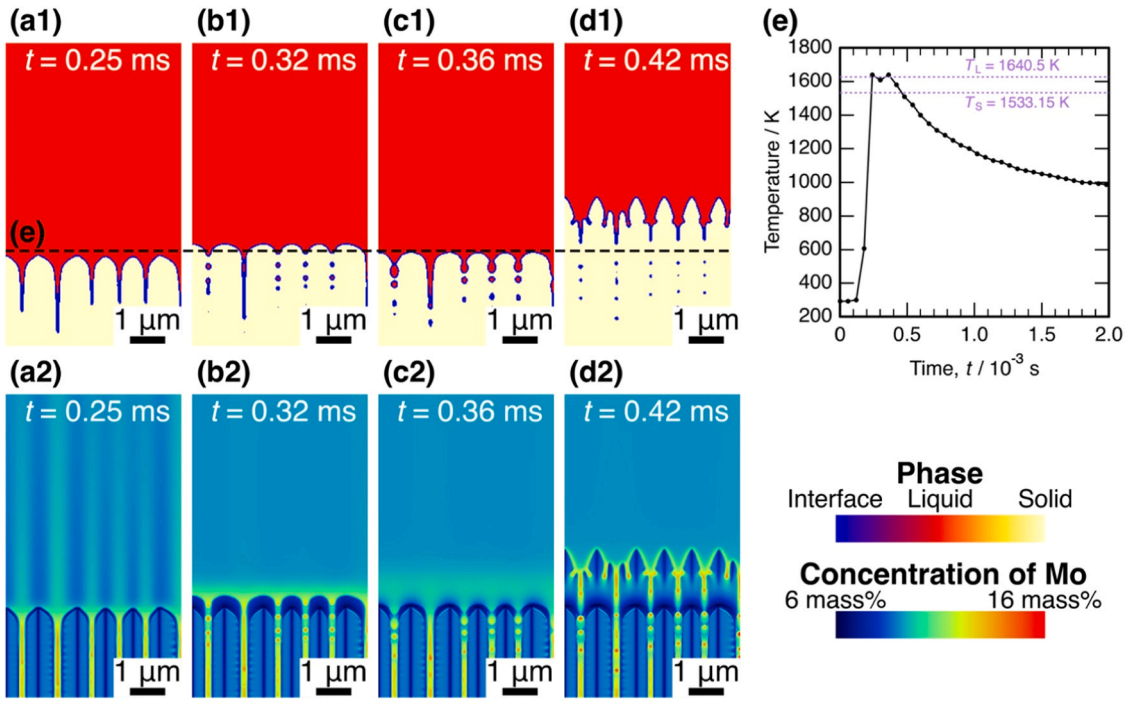

Fig. 9. Snapshots of MPF models during resolidification process colored by the (a1–d1) phase and (a2–d2) Mo concentration. (e) Temperature-time profile at the position indicated by dashed line in (a1–d1).

behavior was significantly affected by remelting and resolidification and varied across the alloy. Solute segregation can be categorized by the regions shown in Fig. 11a1–1a4, namely the cell boundary (Fig. 11a1), interior of the melt-pool boundary (Fig. 11a2), re-remelted regions (Fig. 11a3), and heat-affected regions (Fig. 11a4). The concentration profiles of these regions are shown in Fig. 11b1–11b4. Solute segregation was the highest in the cell boundary region. The solute segregation in the heat-affected region was almost the same as that in the cell boundary region, but seemed to have been attenuated by reheating during remelting and resolidification. The interior of the melt-pool boundary region also had the same tendency for solute segregation. However, the amount of Cr segregation was smaller than that of Mo. A decrease in the Cr concentration was also mitigated, and the concentration remained the same as that in the alloy composition. Fig. 11c1–11c4 show the chemical potentials of the solute elements for the FCC phase at 1073 K calculated using the compositions of those interfacial regions. All the interfacial regions showed non-constant chemical potentials for each element along the perpendicular direction, but the fluctuations of the chemical potentials differed by the type of interfaces. In particular, the fluctuation of the chemical potential of C at the cell boundary region was the largest, suggesting it can be relaxed easily by heat treatment. On the other hand, the fluctuations of the other elements in all the regions were small. The solute segregations are most likely to remain after the heat treatment and are supposed to affect the cracking susceptibilities.

The solidus temperatures T_S, the difference between the liquidus and solidus temperatures (i.e., the brittle temperature range (BTR)), and the fractions of the equilibrium precipitate phases at 1073 K of the interfacial regions were calculated as the liquation, solidification, and ductility dip cracking susceptibilities, respectively. At the cell boundary (Fig. 12a1), interior of the melt-pool boundary (Fig. 12a1), and heat-affected regions (Fig. 12a1), the internal and interfacial regions exhibited higher and lower T_S compared to that of the alloy composition, respectively. The lowest T_s was obtained with the composition at the cell boundary region, which is the largest solute-segregated region. It has been suggested that strong segregations of solute elements in LPBF lead to liquation cracks [16]. This study also supports this suggestion, and liquation cracks are more likely to occur at the interfacial regions indicated by predicting the solute segregation behavior using the MPF model. Additionally, the BTRs of the cell boundary, interior of the melt-pool boundary, and heat-affected regions were wider at the interdendritic regions, and solidification cracks were also likely to occur in these regions. Moreover, within the solute segregation regions, the fraction of the precipitate phases in these interfacial regions was larger than that calculated using the alloy composition (Fig. 12c1, 12c2, and 12c4). This indicates that ductility dip cracking is also likely to occur at the cell boundary, interior of the melt-pool boundary, and in heat-affected regions. Contrarily, we found that the re-remelted region exhibited a higher T_S and smaller BTR even in the interfacial region (Fig. 12a3 and 12b3), where the solute segregation behavior was different from that of the other regions. In addition, the re-remelting region exhibited less precipitation compared with the other segregated regions (Fig. 12c3). The re-remelting caused by the latent heat can attenuate solute segregation, prevent T_s from decreasing, decrease the BTR, and decrease the amount of precipitate phases. Alloys with a large amount of latent heat are expected to increase the re-remelting region, thereby decreasing the susceptibility to liquation and ductility dip cracks due to solute element segregation. This can be a guide for designing alloys for the LPBF process. As mentioned in Section 3.4, the microstructure [45] and the solute segregation behavior [44] at the melt pool boundary of LPBF-manufactured 316 L stainless steel are observed, and they are different from that of the interdendritic regions. Experimental observations of the solute segregation behavior in the LPBF-fabricated Ni-based alloys are currently underway.

4.2. Applicability of the conventional MPF simulation to microstructure formation under LPBF

As the solidification growth rate increases, segregation coefficients approach 1, and the fluctuation of the solid/liquid interface is suppressed by the interfacial tension. The interface growth occurs in a flat fashion instead of having a cellular morphology at a velocity above the absolute stability limit, R_{as}, predicted by the Mullins-Sekerka theory [29]: $R_{as} = (\Delta T_0\, D_L) / (k\, \Gamma)$ where ΔT_0, D_L, k, and Γ are the difference

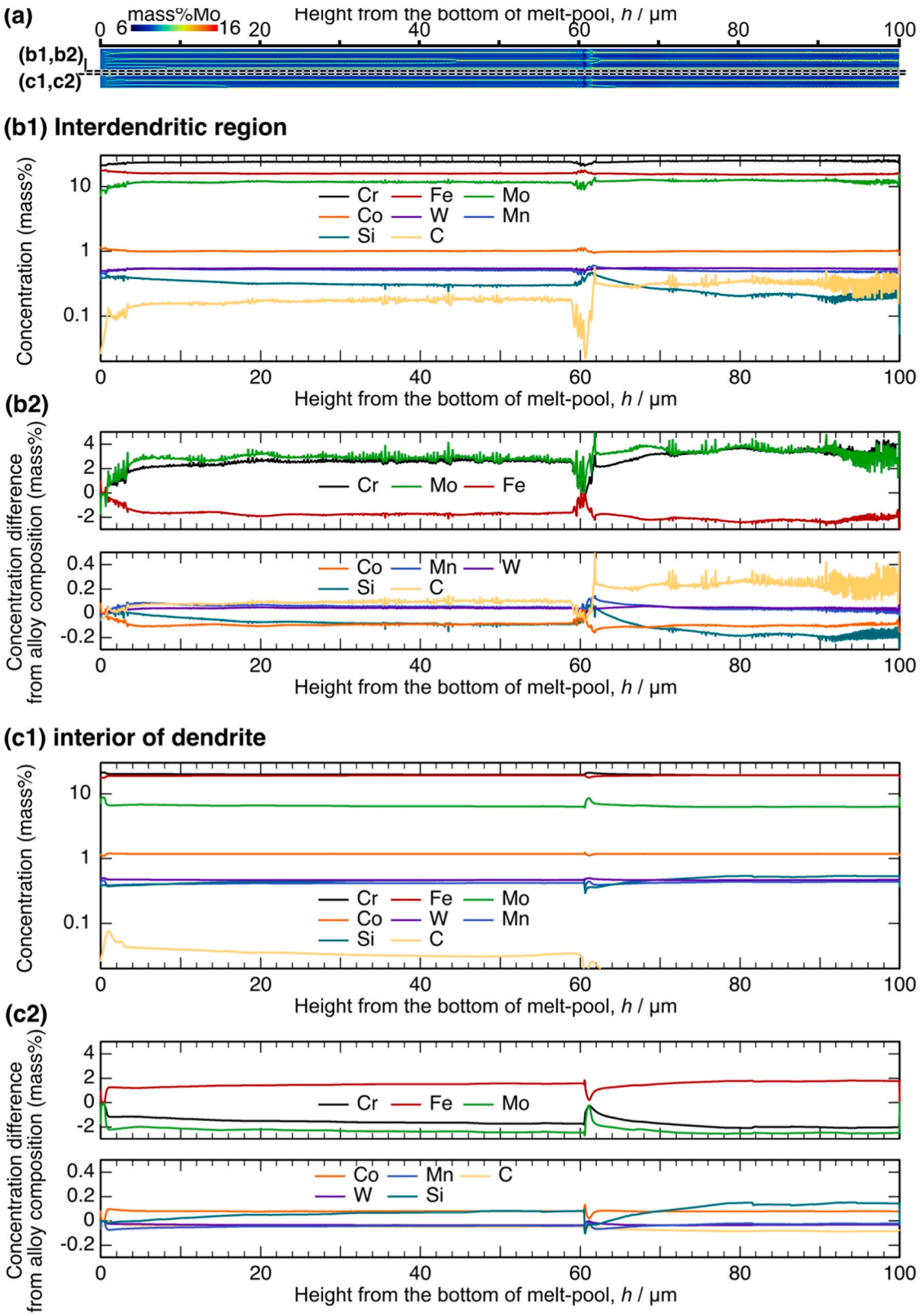

Fig. 10. (a) MPF resolidified model colored by Mo concentration. (b1–c2) Concentration profiles of the MPF resolidified model indicated by dashed lines in (a): (b1, b2) interdendritic region and (c1, c2) interior of the dendrite.

between the liquidus and solidus temperatures, equilibrium segregation coefficient, the diffusivity of liquid, and the Gibbs-Thomson coefficient, respectively.

The R_{as} of HX was calculated using the equation and the thermodynamic parameters obtained by the TCNI9 thermodynamic database [39]. The calculated R_{as} of HX was 3.9 m s^{-1} and is ten times larger than that of the Ni–Nb alloy (approximately 0.4 m s^{-1}) [20]. The HX alloy was solidified under R values in the range of 8.2×10^{-2}–6.3 ×

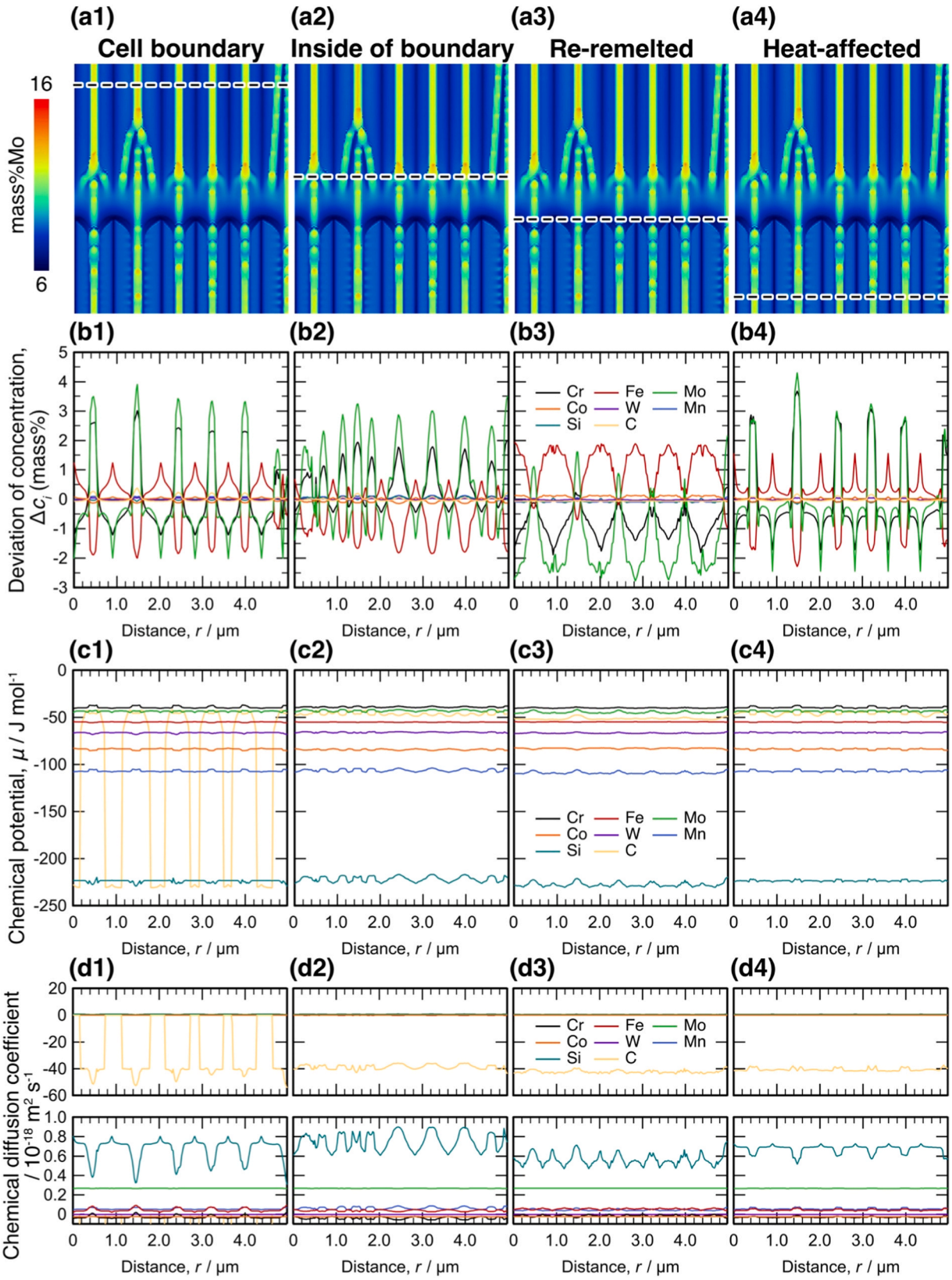

Fig. 11. (a1–a4) MPF models colored by Mo concentration indicating the position of the line along which the profiles in (b) and (c) are obtained; corresponding (b1–b4) segregation profiles, (c1–c4) chemical potentials of each solute element, and (d1–d4) chemical diffusion coefficients.

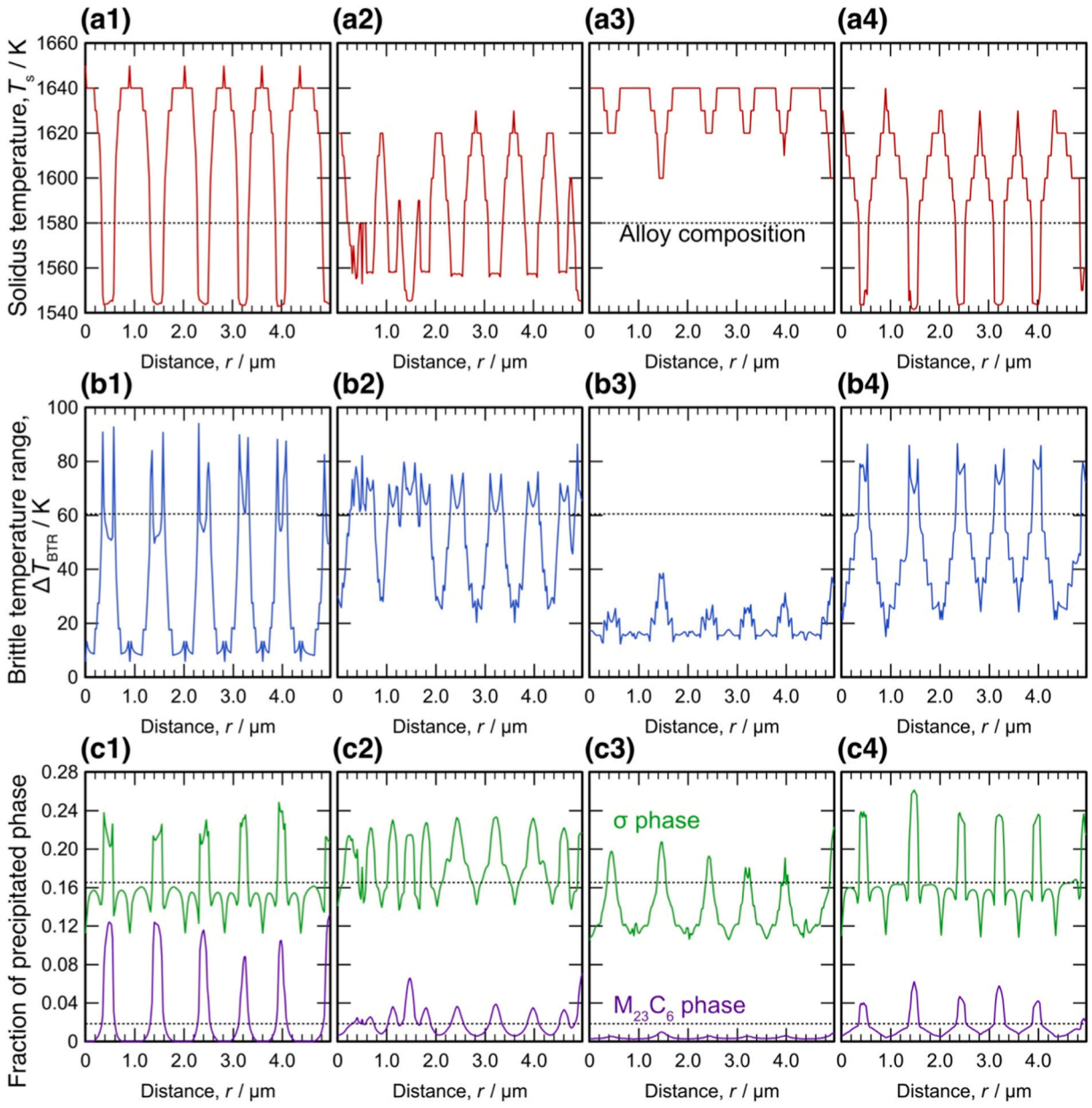

Fig. 12. (a1–a4) The solidus temperatures T_s, (b1–b4) brittle temperature range (BTR), and (c1–c4) fractions of the equilibrium precipitate phases at 1073 K calculated using the compositions at various segregated regions shown in Fig. 11a1–a4.

10^{-1} m s^{-1}. The theoretically calculated criterion is larger than the evaluated R, and is in agreement with the experiment in which dendritic growth is observed in the melt pool (Fig. 5). In contrast, Karayagiz et al. [20] reported that the R of the Ni–Nb binary alloy under LPBF was as high as approximately 2 m s^{-1}, and planar interface growth was observed to be predominant under the high-growth-rate conditions. These experimentally observed microstructures agree well with the prediction by the Mullins-Sekerka theory about the relationship between the morphology and solidification rates.

In this study, the solidification microstructure formed by the laser-beam irradiation of an HX multicomponent Ni-based superalloy was reproduced by a conventional MPF simulation, in which the system was assumed to be in a quasi-equilibrium condition. Boussinot et al. [24] also suggested that the conventional phase-field model can be applied to simulate the microstructure of an IN718 multicomponent Ni-based superalloy in LPBF. In contrast, Kagayaski et al. [20] suggested that the conventional MPF simulation cannot be applied to the solidification of the Ni-Nb binary alloy system and that the finite interface dissipation model proposed by Steinbach et al. [48,49] is necessary to simulate the high solidification rates observed in LPBF. The difference in the applicability of the conventional MPF method to HX and Ni–Nb binary alloys is presumed to arise from the differences in the non-equilibrium degree of these systems under the high solidification rates of LPBF. The results suggest that R_{as} can be used as a simple index to apply the conventional MPF model for solidification in LPBF. Solidification becomes a non-equilibrium process as the solidification rate approaches the limit of absolute stability, R_{as}. In this study, the solidification of the HX multicomponent system occurred under a relatively low solidification rate compared to R_{as}, and the microstructure of the conventional MPF model was successfully reproduced in the physical experiment. However, note that the limit of absolute stability predicted by the Mullins-Sekerka theory was originally proposed for solidification in a binary alloy system, and further investigation is required to consider its applicability to multicomponent alloy systems. Moreover, the fast solidification, such as

in the LPBF process, causes segregation coefficient approaching a value of 1 [20,21,25] corresponds to a diffusion length that is on the order of the atomic interface thickness. When the segregation coefficient approaches 1, solute undercooling disappears; hence, there is no driving force to amplify fluctuations regardless of whether interfacial tension is present. This phenomenon should be further investigated in future studies.

5. Conclusions

We simulated solute segregation in a multicomponent HX alloy under the LPBF process by an MPF simulation using the temperature distributions obtained by a CtFD simulation. We set the parameters of the CtFD simulation to match the melt pool shape formed in the laser-irradiation experiment and found that solidification occurred under high cooling rates of up to 1.6×10^6 K s^{-1}.

MPF simulations using the temperature distributions from CtFD simulation could reproduce the experimentally observed PDAS and revealed that significant solute segregation occurred at the interdendritic regions. Equilibrium thermodynamic calculations using the alloy compositions of the segregated regions when considering crack sensitivities suggested a decrease in the solidus temperature and an increase in the amount of carbide precipitation, thereby increasing the susceptibility to liquation and ductility dip cracks in these regions. Notably, these changes were suppressed at the melt-pool boundary region, where re-remelting occurred during the stacking of the layer above. This effect can be used to achieve a novel in-process segregation attenuation.

Our study revealed that a conventional MPF simulation weakly coupled with a CtFD simulation can be used to study the solidification of multicomponent alloys in LPBF, contrary to the cases of binary alloys investigated in previous studies. We discussed the applicability of the conventional MPF model to the LPBF process in terms of the limit of absolute stability, R_{as}, and suggested that alloys with a high limit velocity, i.e., multicomponent alloys, can be simulated using the conventional MPF model even under the high solidification velocity conditions of LPBF.

CRediT authorship contribution statement

Masayuki Okugawa: Writing – review & editing, Writing – original draft, Visualization, Validation, Software, Methodology, Investigation, Formal analysis, Data curation, Conceptualization. **Takayoshi Nakano:** Writing – review & editing, Validation, Supervision, Funding acquisition. **Yuichiro Koizumi:** Writing – review & editing, Visualization, Validation, Supervision, Project administration, Methodology, Investigation, Funding acquisition, Formal analysis, Data curation, Conceptualization. **Sukeharu Nomoto:** Writing – review & editing, Validation, Investigation. **Makoto Watanabe:** Writing – review & editing, Validation, Supervision, Funding acquisition. **Katsuhiko Sawaizumi:** Validation, Software, Investigation, Formal analysis, Data curation. **Kenji Saito:** Visualization, Validation, Software, Methodology, Investigation, Formal analysis, Data curation. **Haruki Yoshima:** Visualization, Validation, Software, Investigation, Formal analysis, Data curation.

Declaration of Competing Interest

The authors declare that they have no known competing financial interests or personal relationships that could have appeared to influence the work reported in this paper

Data availability

Data will be made available on request.

Acknowledgments

This work was partly supported by the Cabinet Office, Government of Japan, Cross-ministerial Strategic Innovation Promotion Program (SIP), “Materials Integration for Revolutionary Design System of Structural Materials,” (funding agency: The Japan Science and Technology Agency), by JSPS KAKENHI Grant-in-Aid for Transformative Research Areas (A) “Creation of Materials by Super Thermal Field: Neo-3D printing by Manipulating Atomic Arrangement through Giant Potential Gradient” (Grant Numbers 21H05018 and 21H05193), and by CREST Nanomechanics: Elucidation of macroscale mechanical properties based on understanding nanoscale dynamics for innovative mechanical materials (Grant Number: JPMJCR2194) from the Japan Science and Technology Agency (JST). The authors would like to thank Mr. H. Kawabata and Mr. K. Kimura for their technical support with the sample preparations and laser beam irradiation experiments.

Appendix A. Supporting information

Supplementary data associated with this article can be found in the online version at doi:10.1016/j.addma.2024.104079.

References

[1] M. Ramsperger, R.F. Singer, C. Körner, Microstructure of the nickel-base superalloy CMSX-4 fabricated by selective electron beam melting, Metall. Mater. Trans. A Phys. Metall. Mater. Sci. 47 (2016) 1469–1480, https://doi.org/10.1007/s11661-015-3300-y.

[2] J.H. Martin, B.D. Yahata, J.M. Hundley, J.A. Mayer, T.A. Schaedler, T.M. Pollock, 3D printing of high-strength aluminium alloys, Nature 549 (2017) 365–369, https://doi.org/10.1038/nature23894.

[3] K. Hagihara, T. Nakano, Control of anisotropic crystallographic texture in powder bed fusion additive manufacturing of metals and ceramics—a review, JOM 74 (2021) 1760–1773, https://doi.org/10.1007/s11837-021-04966-7.

[4] Y. Koizumi, M. Okugawa, Digital twin science of metal powder bed fusion additive manufacturing: a selective review of simulations for integrated computational materials engineering and science, ISIJ Int 62 (2022) 2183–2196, https://doi.org/10.2355/isijinternational.ISIJINT-2022-184.

[5] S. Ghosh, J. Zollinger, M. Zaloznik, D. Banerjee, C.K. Newman, R. Arroyave, Modeling of hierarchical solidification microstructures in metal additive manufacturing: challenges and opportunities, Addit. Manuf. 78 (2023) 103845, https://doi.org/10.1016/j.addma.2023.103845.

[6] N. Raghavan, R. Dehoff, S. Pannala, S. Simunovic, M. Kirka, J. Turner, N. Carlson, S.S. Babu, Numerical modeling of heat-transfer and the influence of process parameters on tailoring the grain morphology of IN718 in electron beam additive manufacturing, Acta Mater. 112 (2016) 303–314, https://doi.org/10.1016/j.actamat.2016.03.063.

[7] N. Raghavan, S. Simunovic, R. Dehoff, A. Plotkowski, J. Turner, M. Kirka, S. Babu, Localized melt-scan strategy for site specific control of grain size and primary dendrite arm spacing in electron beam additive manufacturing, Acta Mater. 140 (2017) 375–387, https://doi.org/10.1016/j.actamat.2017.08.038.

[8] O. Gokcekaya, T. Ishimoto, S. Hibino, J. Yasutomi, T. Narushima, T. Nakano, Unique crystallographic texture formation in Inconel 718 by laser powder bed fusion and its effect on mechanical anisotropy, Acta Mater. 212 (2021) 116876, https://doi.org/10.1016/j.actamat.2021.116876.

[9] T. Keller, G. Lindwall, S. Ghosh, L. Ma, B.M. Lane, F. Zhang, U.R. Kattner, E.A. Lass, J.C. Heigel, Y. Idell, M.E. Williams, A.J. Allen, J.E. Guyer, L.E. Levine, Application of finite element, phase-field, and CALPHAD-based methods to additive manufacturing of Ni-based superalloys, Acta Mater. 139 (2017) 244–253, https://doi.org/10.1016/j.actamat.2017.05.003.

[10] F. Zhang, L.E. Levine, A.J. Allen, M.R. Stoudt, G. Lindwall, E.A. Lass, M. E. Williams, Y. Idell, C.E. Campbell, Effect of heat treatment on the microstructural evolution of a nickel-based superalloy additive-manufactured by laser powder bed fusion, Acta Mater. 152 (2018) 200–214, https://doi.org/10.1016/j.actamat.2018.03.017.

[11] N.J. Harrison, I. Todd, K. Mumtaz, Reduction of micro-cracking in nickel superalloys processed by selective laser melting: a fundamental alloy design approach, Acta Mater. 94 (2015) 59–68, https://doi.org/10.1016/j.actamat.2015.04.035.

[12] H. Wang, L. Chen, B. Dovgyy, W. Xu, A. Sha, X. Li, H. Tang, Y. Liu, H. Wu, M. S. Pham, Micro-cracking, microstructure and mechanical properties of Hastelloy-X alloy printed by laser powder bed fusion: as-built, annealed and hot-isostatic pressed, Addit. Manuf. 39 (2021) 101853, https://doi.org/10.1016/j.addma.2021.101853.

[13] D. Tomus, P.A. Rometsch, M. Heilmaier, X. Wu, Effect of minor alloying elements on crack-formation characteristics of Hastelloy-X manufactured by selective laser melting, Addit. Manuf. 16 (2017) 65–72, https://doi.org/10.1016/j.addma.2017.05.006.

[14] H. Kitano, M. Tsujii, M. Kusano, A. Yumoto, M. Watanabe, Effect of plastic strain on the solidification cracking of Hastelloy-X in the selective laser melting process, Addit. Manuf. 37 (2020) 101742, https://doi.org/10.1016/j.addma.2020.101742.
[15] J. Xu, H. Gruber, D. Deng, R.L. Peng, J.J. Moverare, Short-term creep behavior of an additive manufactured non-weldable Nickel-base superalloy evaluated by slow strain rate testing, Acta Mater. 179 (2019) 142–157, https://doi.org/10.1016/j.actamat.2019.08.034.
[16] P. Kontis, E. Chauvet, Z. Peng, J. He, A.K. da Silva, D. Raabe, C. Tassin, J. J. Blandin, S. Abed, R. Dendievel, B. Gault, G. Martin, Atomic-scale grain boundary engineering to overcome hot-cracking in additively-manufactured superalloys, Acta Mater. 177 (2019) 209–221, https://doi.org/10.1016/j.actamat.2019.07.041.
[17] C. Körner, M. Ramsperger, C. Meid, D. Bürger, P. Wollgramm, M. Bartsch, G. Eggeler, Microstructure and mechanical properties of CMSX-4 single crystals prepared by additive manufacturing, Metall. Mater. Trans. A Phys. Metall. Mater. Sci. 49 (2018) 3781–3792, https://doi.org/10.1007/s11661-018-4762-5.
[18] T. Ishimoto, R. Ozasa, K. Nakano, M. Weinmann, C. Schnitter, M. Stenzel, A. Matsugaki, T. Nagase, T. Matsuzaka, M. Todai, H.S. Kim, T. Nakano, Development of TiNbTaZrMo bio-high entropy alloy (BioHEA) super-solid solution by selective laser melting, and its improved mechanical property and biocompatibility, Scr. Mater. 194 (2021) 113658, https://doi.org/10.1016/j.scriptamat.2020.113658.
[19] M. Okugawa, D. Izumikawa, Y. Koizumi, Simulations of non-equilibrium and equilibrium segregation in nickel-based superalloy using modified Scheil-Gulliver and phase-field methods, Mater. Trans. 61 (2020) 2072–2078, https://doi.org/10.2320/matertrans.mt-ma2020005.
[20] K. Karayagiz, L. Johnson, R. Seede, V. Attari, B. Zhang, X. Huang, S. Ghosh, T. Duong, I. Karaman, A. Elwany, R. Arróyave, Finite interface dissipation phase field modeling of Ni–Nb under additive manufacturing conditions, Acta Mater. 185 (2020) 320–339, https://doi.org/10.1016/j.actamat.2019.11.057.
[21] S. Ghosh, L. Ma, N. Ofori-Opoku, J.E. Guyer, On the primary spacing and microsegregation of cellular dendrites in laser deposited Ni-Nb alloys, Model. Simul. Mater. Sci. Eng. 25 (2017), https://doi.org/10.1088/1361-651X/aa7369.
[22] S. Nomoto, M. Segawa, M. Watanabe, Non- and quasi-equilibrium multi-phase field methods coupled with CALPHAD database for rapid-solidification microstructural evolution in laser powder bed additive manufacturing condition, Metals 11 (2021) 626, https://doi.org/10.3390/met11040626.
[23] J. Kundin, L. Mushongera, H. Emmerich, Phase-field modeling of microstructure formation during rapid solidification in Inconel 718 superalloy, Acta Mater. 95 (2015) 343–356, https://doi.org/10.1016/j.actamat.2015.05.052.
[24] G. Boussinot, M. Apel, J. Zielinski, U. Hecht, J.H. Schleifenbaum, Strongly out-of-equilibrium columnar solidification during laser powder-bed fusion in additive manufacturing, Phys. Rev. Appl. 11 (2019) 014025, https://doi.org/10.1103/PhysRevApplied.11.014025.
[25] K. Ji, E. Dorari, A.J. Clarke, A. Karma, Microstructural pattern formation during far-from-equilibrium alloy solidification, Phys. Rev. Lett. 130 (2022) 26203, https://doi.org/10.1103/PhysRevLett.130.026203.
[26] M. Okugawa, Y. Ohigashi, Y. Furishiro, Y. Koizumi, T. Nakano, Equiaxed grain formation by intrinsic heterogeneous nucleation via rapid heating and cooling in additive manufacturing of aluminum-silicon hypoeutectic alloy, J. Alloy. Compd. 919 (2022) 165812, https://doi.org/10.1016/j.jallcom.2022.165812.
[27] M. Okugawa, Y. Furushiro, Y. Koizumi, Effect of rapid heating and cooling conditions on microstructure formation in powder bed fusion of Al-Si hypoeutectic alloy: a phase-field study, Materials 15 (2022) 6092, https://doi.org/10.3390/ma15176092.
[28] R. Acharya, J.A. Sharon, A. Staroselsky, Prediction of microstructure in laser powder bed fusion process, Acta Mater. 124 (2017) 360–371, https://doi.org/10.1016/j.actamat.2016.11.018.
[29] M. Rappaz, J.A. Dantzig. Solidification, first ed., EFPL Press, Lausanne, 2009.
[30] S.M. Elahi, R. Tavakoli, A.K. Boukellal, T. Isensee, I. Romero, D. Tourret, Multiscale simulation of powder-bed fusion processing of metallic alloys, Comput. Mater. Sci. 209 (2022) 111383, https://doi.org/10.1016/j.commatsci.2022.111383.
[31] C. Tang, J.L. Tan, C.H. Wong, A numerical investigation on the physical mechanisms of single track defects in selective laser melting, Int. J. Heat. Mass Transf. 126 (2018) 957–968, https://doi.org/10.1016/j.ijheatmasstransfer.2018.06.073.
[32] Technical Data for Nickel. Available online: ⟨https://periodictable.com/Elements/028/data.html⟩ (accessed on 16 January 2023).
[33] MICRostructure Evolution Simulation Software, Phase-Field Software Package. Available online: ⟨https://micress.rwth-aachen.de⟩ (accessed on 24 March 2023).
[34] J. Eiken, B. Böttger, I. Steinbach, Multiphase-field approach for multicomponent alloys with extrapolation scheme for numerical application, Phys. Rev. E - Stat. Nonlinear, Soft Matter Phys. 73 (2006) 1–9, https://doi.org/10.1103/PhysRevE.73.066122.
[35] B. Böttger, M. Apel, M. Budnitzki, J. Eiken, G. Laschet, B. Zhou, Calphad coupled phase-field model with mechano-chemical contributions and its application to rafting of γ' in CMSX-4, Comput. Mater. Sci. 184 (2020) 109909, https://doi.org/10.1016/j.commatsci.2020.109909.
[36] C. Kumara, A. Ramanathan Balachandramurthi, S. Goel, F. Hanning, J. Moverare, Toward a better understanding of phase transformations in additive manufacturing of Alloy 718, Materialia 13 (2020) 100862.
[37] B. Böttger, M. Apel, Phase-field simulation of the formation of new grains by fragmentation during melting of an ABD900 superalloy, IOP Conf. Ser. Mater. Sci. Eng. 1281 (2023) 012008, https://doi.org/10.1088/1757-899x/1281/1/012008.
[38] J.O. Andersson, T. Helander, L. Höglund, P. Shi, B. Sundman, Thermo-Calc & DICTRA, computational tools for materials science, Calphad 26 (2002) 273–312, https://doi.org/10.1016/S0364-5916(02)00037-8.
[39] Thermo-Calc Software, Ni-Based Superalloys Database, Version 9. URL, ⟨http://www.thermocalc.com/products-services/databases/thermodynamic/⟩.
[40] Thermo-Calc Software, Ni-alloys Mobility Database, Version 5. URL, ⟨https://www.thermocalc.com/products-services/databases/mobility/⟩.
[41] J.C. Zhao, M. Larsen, V. Ravikumar, Phase precipitation and time-temperature-transformation diagram of Hastelloy X, Mater. Sci. Eng. A. 293 (2000) 112–119, https://doi.org/10.1016/S0921-5093(00)01049-2.
[42] M. Ode, S.G. Kim, W.T. Kim, T. Suzuki, Numerical prediction of the secondary dendrite arm spacing using a phase-field model, ISIJ Int 41 (2001) 345–349, https://doi.org/10.2355/isijinternational.41.345.
[43] S. Banoth, T.N. Palleda, T. Saito, H. Murakami, K. Kakehi, Effects of yttrium and silicon contents in Hastelloy-X built by selective laser melting process, J. Alloy. Compd. 896 (2022) 163050, https://doi.org/10.1016/j.jallcom.2021.163050.
[44] K. Sato, S. Takagi, S. Ichikawa, T. Ishimoto, T. Nakano, Microstructure and solute segregation around the melt-pool boundary of orientation-controlled 316L austenitic stainless steel produced by laser powder bed fusion, Materials 16 (2023), https://doi.org/10.3390/ma16010218.
[45] Y. Liu, K. Nose, M. Okugawa, Y. Koizumi, T. Nakano, Fabrication and process monitoring of 316L stainless steel by laser powder bed fusion with μ-helix scanning strategy and narrow scanning line intervals, Mater. Trans. 64 (2023) 1135–1142, https://doi.org/10.2320/matertrans.MT-ME2022006.
[46] H. Schaar, I. Steinbach, M. Tegeler, Numerical study of epitaxial growth after partial remelting during selective electron beam melting in the context of Ni–Al, Metals 11 (2021) 2–13, https://doi.org/10.3390/met11122012.
[47] M. Uddagiri, O. Shchyglo, I. Steinbach, B. Wahlmann, C. Koerner, Phase-field study of the history-effect of remelted microstructures on nucleation during additive manufacturing of Ni-based superalloys, Metall. Mater. Trans. A Phys. Metall. Mater. Sci. 54 (2023) 1825–1842, https://doi.org/10.1007/s11661-023-07004-0.
[48] I. Steinbach, L. Zhang, M. Plapp, Phase-field model with finite interface dissipation, Acta Mater. 60 (2012) 2689–2701, https://doi.org/10.1016/j.actamat.2012.01.035.
[49] L. Zhang, I. Steinbach, Phase-field model with finite interface dissipation: Extension to multi-component multi-phase alloys, Acta Mater. 60 (2012) 2702–2710, https://doi.org/10.1016/j.actamat.2012.02.032.